

Ultraviolet Imaging Telescope (UVIT) observation of the Galactic Globular Cluster NGC 7492

Ranjan Kumar,¹★ Ananta C. Pradhan,¹† Abhisek Mohapatra,¹ Ayush Moharana,^{1,2}
Devendra K. Ojha,³ M. Parthasarathy,⁴ and Jayant Murthy⁴

¹Department of Physics and Astronomy, National Institute of Technology, Rourkela, Odisha - 769 008, India

²Nicolaus Copernicus Astronomical Center, Polish Academy of Sciences, ul. Rabiniańska 8, 87-100 Toruń, Poland

³Department of Astronomy and Astrophysics, Tata Institute of Fundamental Research (TIFR), Mumbai - 400 005, India

⁴Indian Institute of Astrophysics, Bangalore - 560 034, India

Accepted 2020 December 22. Received 2020 December 22; in original form 2020 March 13

ABSTRACT

We present detailed photometric observations of the Galactic globular cluster NGC 7492 using the data obtained with two far-ultraviolet (FUV: 1300 - 1800 Å) and three near-ultraviolet (NUV: 2000 - 3000 Å) filters of Ultraviolet Imaging Telescope (UVIT) on-board the *AstroSat* satellite. We confirmed the cluster membership of the extracted sources using GAIA data release 2 (Gaia DR2) proper motion data. We have used color-magnitude diagrams (CMDs) using UVIT and GAIA filters to separate out different evolutionary stages of the stars present in the cluster. We have identified a new extreme horizontal branch (EHB) star at the core of the cluster using UV and UV-optical CMDs. The estimated distance-modulus of the cluster is 16.95 ± 0.05 obtained by fitting BaSTI isochrones with cluster parameters, $[Fe/H] = -1.8$ dex and age = 12.0 Gyr on the V - I vs V CMD. Interestingly, only the EHB star and blue horizontal branch stars (BHBs) among the UV-bright hot sources are detected in FUV filters of UVIT. We have derived the effective temperature of BHBs using color-temperature relation and spectral energy distributions (SEDs) of multi-band filters, which are in the range from 8,000 K to 10,500 K. We find a variation of He abundance of BHBs by fitting the BaSTI ZAHB. The range in the He abundance of the BHBs corresponding to the best fit isochrones is 0.247 to 0.350. We have estimated various physical parameters of the newly identified EHB star in the cluster using SED fit and post-HB evolutionary tracks. We have studied the radial distribution of all the sources of the cluster detected in UVIT. The sources detected in FUV filters extend beyond the half light radius (1.15') of the cluster, whereas the sources detected in NUV filters extend beyond the tidal radius (9.2') of the cluster.

Key words: ultraviolet: stars - (Galaxy:) globular clusters: individual: NGC 7492 - stars: horizontal branch, stars: evolution, (stars:) Hertzsprung-Russell and colour-magnitude diagrams

1 INTRODUCTION

Galactic globular clusters (GGCs) are comprised of old stellar populations which are crucial to understand the stellar evolution as well as numerous peculiar properties of the Milky Way Galaxy. GGCs also help in constraining the structural, kinematical and dynamical properties of the Galactic halo (Harris & Racine 1979; Freeman & Norris 1981; Rosenberg 2000; Keller et al. 2012; Arakelyan et al. 2018; Posti & Helmi 2019; Kruijssen et al. 2019; Massari et al. 2019). They are relatively proximate objects consisting of a huge number of coeval stars with less interstellar extinction which allows

to explore the various evolutionary phases of individual stars. Subsequently, a detailed study of different stellar populations provides clues about the formation and evolution of GGCs (Ferraro 2003; Tenorio-Tagle et al. 2016, 2019).

The ultraviolet (UV) light in GGCs is due to the hot, bright sources such as post-asymptotic giant branch stars (pAGB), blue straggler stars (BSs), extreme blue and blue horizontal branch stars (EHBs, BHBs), white dwarfs (WDs), etc. Many studies have performed photometric and spectroscopic analysis of these sources, which dominate the total integrated light of the GGCs in the UV (Zinn et al. 1972; Harris et al. 1983; Moehler et al. 1998; Ambika et al. 2004; Jasiewicz et al. 2004; Moehler 2010; Dalessandro et al. 2011; Schiavon et al. 2012; Dalessandro et al. 2013; Piotto et al. 2015; Subramaniam et al. 2017; Sahu et al. 2019; Moehler et al.

★ E-mail: ranjankmr488@gmail.com

† E-mail: acp.phy@gmail.com

2019). The UV bright stars in globular clusters also serve as standard candles because they have same absolute luminosity over a wide range of effective temperature (T_{eff}) values (Bond & Alves 2001; Jasiewicz & Parthasarathy 2009; Parthasarathy et al. 2012). A comprehensive and homogeneous database of magnitudes and colors of the UV bright sources for a good number of GGCs has been cataloged using observations from *Galaxy Evolution Explorer* (GALEX) (Schiavon et al. 2012; Dalessandro et al. 2012), and the *Hubble Space Telescope* (HST) (Piotto et al. 2015; Lagioia et al. 2015). Ultraviolet Imaging Telescope (UVIT) with unprecedented resolution is providing a very good opportunity to collect UV data of GGCs to unravel the complexities involved in the UV properties of the stars at the end stage of their evolution. Recently, the UV properties of a list of GGCs have been explored using UVIT observations (Subramaniam et al. 2017; Sahu et al. 2019; Jain et al. 2019; Kumar et al. 2020a,b). The authors have identified multiple stellar populations in GGCs and subsequently studied their distributions and properties using multi-band filters of UVIT.

GGCs have been classified from class I - XII based on the concentration of sources towards their centers (Shapley 1918; Shapley & Sawyer 1927). NGC 7492 is a sparse Galactic halo globular cluster, classified as class 'XII', as the distribution of the sources in the cluster are not strongly concentrated in the center of the cluster. It is situated at a heliocentric distance of about 26.3 ± 2.3 kpc (Cote et al. 1991; Figuera Jaimes et al. 2013; Carballo-Bello et al. 2018) with Galactic coordinates, $l = 53.39^\circ$ and $b = -63.48^\circ$. The age and metallicity ($[Fe/H]$) of the cluster are about 12 ± 0.5 Gyr and -1.8 ± 0.3 dex, respectively (Cohen & Melendez 2005; Forbes & Bridges 2010; Harris 2010; Figuera Jaimes et al. 2013). The latest 3D extinction map of Green et al. (2019) gives the amount of visual extinction in the cluster direction at a distance of 25 kpc to be $E(B - V) = 0.04$ mag. The overall shape of NGC 7492 is flattened with a tail like structure around it as predicted by Lee et al. (2004) and latter confirmed by Navarrete et al. (2017) using the data of Pan-STARRS survey. Since, the cluster lies together with the stellar streams of the Sagittarius dwarf galaxy, it was predicted that the origin of the cluster might be from the Sagittarius dwarf galaxy but further investigations ruled out this claim (Carballo-Bello et al. 2014, 2018).

The UV bright sources in NGC 7492 have several studies in optical bands (Buonanno et al. 1987; Cote et al. 1991; Lee et al. 2004; Carballo-Bello et al. 2012; Figuera Jaimes et al. 2013) prior to their analysis in UV using GALEX observation (Schiavon et al. 2012; Dalessandro et al. 2012). A uniform distribution of BHBs was suggested by Buonanno et al. (1987) at the core of the cluster without any extended blue tails (i.e., no EHBs). Navarrete et al. (2017) with a Pan-STARRS wide field imaging survey found the presence of BHBs in the extended tidal arms of the cluster. Cote et al. (1991) identified 27 BSs within the cluster which were predicted to be formed due to mass segregation in the cluster. So far, seven variable sources (three RR Lyraes, two SX Phoenixis (SXPhes) and two long period variables) have been discovered in the cluster in optical bands (Shapley 1920; Barnes 1968; Figuera Jaimes et al. 2013).

There are only a few studies of the cluster in UV bands, all using the GALEX observations (Schiavon et al. 2012; Dalessandro et al. 2012). They have provided UV CMDs for the detected UV-bright sources and integrated magnitude of the cluster. Their study was focused far off the central region of the cluster owing to the crowding effect and also they did not compare the observations with stellar evolutionary models. UVIT with superior resolution ($\sim 1.5''$) than GALEX ($\sim 4.5''$), has the ability to resolved the central

part of the cluster establishing its better capabilities to study the GGCs. UVIT observation of the cluster has enabled us to constrain the cluster parameters by comparing stellar evolutionary models to observations. With the intention of providing multi-band UV photometric properties of this cluster, we have observed NGC 7492 in five different filters of UVIT. In this paper, we present a detailed UV photometric analysis of NGC 7492 using two far-UV (FUV) and three near-UV (NUV) filters of UVIT on-board the Indian satellite *AstroSat*.

In Section 2, we present the observation details, data reduction process and photometry of the detected sources. In section 3, we show the CMDs of all the detected sources. In Section 4, we estimate the distance of the cluster and the He abundance of the BHBs. In Section 5, we discuss about the estimation of T_{eff} of the BHBs. In Section 6, we derive the various physical parameters of the newly identified EHB star. In Section 7, we have discussed the spatial distribution of various sources, and then we summarize our results in Section 8.

2 OBSERVATIONS AND DATA REDUCTION

2.1 Observations

We have observed NGC 7492 with the UVIT instrument on-board the *AstroSat* satellite. UVIT consists of 38 cm twin telescopes: one observes in the FUV (1300 - 1800 Å) and the other in the NUV (2000 - 3000 Å) and visible (3200 - 5500 Å) bands using a dichroic mirror beam-splitter. The FUV and NUV channels have five filters each for imaging purpose in photon counting mode. The visible channel has five filters, observing in an integrating mode, but is primarily used for tracking purposes. The field of view (FoV) of UVIT is $30'$ with image pixel size of $0.417''/\text{pixel}$. The point spread functions (PSFs) of FUV and NUV filters are $1.5''$ and $1.2''$, respectively (Tandon et al. 2017; Rahna et al. 2017). The filter specifications of UVIT are available in UVIT - *AstroSat* web-page¹, whereas the instrumentation and ground based calibration are given in Kumar et al. (2012a,b). The on-board performance verification and in-orbits calibrations of various filters of UVIT can be found in Subramaniam et al. (2016); Tandon et al. (2017); Rahna et al. (2017); Tandon et al. (2020).

We obtained observations with two FUV filters (BaF2 and Silica) and three NUV filters (NUVB15, NUVB13 and NUVB4) of UVIT with exposure times of 0.347 ks to 3.276 ks, depending on the filter, in the A02 cycle of observation (Observation ID: A02_72, PI: Ananta C. Pradhan). The observational details are given in Table 1.

2.2 Data Reduction

The data reduction of UVIT observation was performed with the software package CCDLAB, written specifically for UVIT data by Postma & Leahy (2017). CCDLAB converts the Level 1 data, obtained from the Indian Space Science Data Centre (ISSDC), into astronomical images for each orbit of the five filters. We then aligned and co-added all the orbits of a filter to obtain its corresponding science image to perform the photometry. We applied astrometry from GAIA DR2 catalog (Gaia Collaboration et al. 2018a) using IRAF *ccmap* package.

In Figure 1, we have compared the UVIT NUVB4 image of the crowded core region of NGC 7492 with that of GALEX NUV

¹ <https://uvit.iap.res.in/Instrument/Filters>

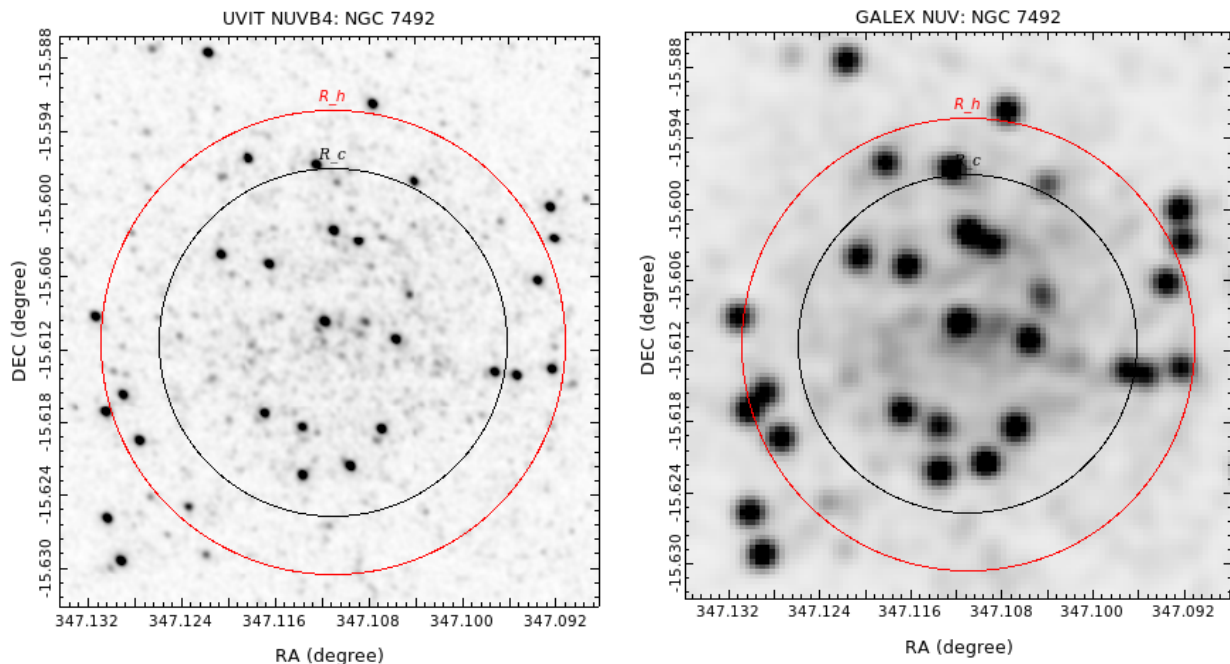


Figure 1. UVIT NUVB4 ($\lambda_{\text{eff}} = 2632 \text{ \AA}$, left) and GALEX NUV ($\lambda_{\text{eff}} = 2304 \text{ \AA}$, right) images of NGC 7492. The red circle denotes the half light radius ($R_h = 1.15'$) and the black circle denotes the core radius ($R_c = 0.86'$) of the cluster (Harris 2010).

Table 1. Observational details of NGC 7492.

Date of observation	2016, October 19			
Telescope pointing	$l = 53.4^\circ$, $b = -63.5^\circ$			
Filter	mean λ (\AA)	$\Delta\lambda$ (\AA)	Exposure Time (sec.)	No. of orbits
NUVB4	2632	275	3014	3
NUVB13	2447	280	3276	3
NUVB15	2196	270	347	1
Silica	1717	125	850	2
BaF2	1541	380	349	1

filter. The exposure time of UVIT NUVB4 filter is 3014 seconds and that for GALEX NUV filter is 3200 seconds (Schiavon et al. 2012). We clearly see the effect of high resolution of UVIT ($\sim 1.5''$) over GALEX ($\sim 4.5''$), as UV bright sources have been better resolved within the half light radius of the cluster ($R_h = 1.15'$; Harris 2010). We see three bright sources, which are not resolved in GALEX image (right panel, Figure 1), whereas these sources are clearly separable in UVIT image (left panel, Figure 1).

2.3 Photometry

We have performed photometry using the IRAF DAOPHOT package which selects a few isolated sources from the image and develops a PSF model. The model PSF is applied to all the detected sources in order to perform photometry on the entire image. We used the following steps to obtain photometry on the observed images. We generated the model PSF using 20–25 isolated sources in each filter image. An average FWHM of $1.7''$ and $1.5''$ for the PSF model was obtained for the FUV and NUV filter images, respectively. We used these values to perform aperture photometry. The model PSF and aperture photometry were incorporated into the ALLSTAR routine to obtain the final PSF magnitudes of the detected sources. We performed a curve of growth analysis on PSF modeled sources to obtain

an aperture correction value which was applied to the PSF magnitudes of the sources. Then a final catalog of apparent magnitudes for the detected sources of NGC 7492 was obtained in the FUV and NUV filters. The magnitudes of the sources in the UVIT filters were corrected for extinction values, which were estimated using Cardelli et al. (1989) extinction law and A_V values from Green et al. (2019).

2.4 Other archival data

We have used several available archival observations of the cluster for the study of CMDs and spectral energy distribution (SED) fitting of UVIT detected sources. We have obtained the proper motions (μ_{RA} , μ_{DEC}) and G, BP and RP band magnitudes for sources using Gaia Data Release 2 (Gaia DR2, Gaia Collaboration et al. 2018a). Apart from the Gaia DR2 data, we have also used GALEX, Canada-France-Hawaii Telescope (CFHT), Panoramic Survey Telescope and Rapid Response System (PanSTARRs), and ground based UVRI observations for the comprehensive analysis of the sources contained in the cluster within the UVIT FoV. In order to make a comparative study of GALEX observations with UVIT, we collected GALEX images of the cluster from the Mikulski Archive for Space Telescopes (MAST) site and the FUV and NUV magnitudes from Schiavon et al. (2012)². Similarly, we have used two filters, g and r of CFHT observation (Muñoz et al. 2018) and five filters (g, r, i, y, and z) of PanSTARRs-PS1 survey data (Chambers et al. 2016) for the SED fitting of BHBs. We have also adopted data in U, B, V, R and I filters from the latest released ground based archival data of the cluster (Stetson et al. 2019) to study the UV-optical CMDs and SED fittings of BHBs.

² <http://www.cosmic-lab.eu/uvggc/archive.php>

2.5 Cluster membership with Gaia DR2 proper motion

Recent works use Gaia DR2 proper motion catalog to identify the cluster members in GGCs (Gaia Collaboration et al. 2018b; Vasiliev 2019; Baumgardt et al. 2019; Bustos Fierro & Calderón 2019). Generally, proper motions in RA (μ_{RA}) and DEC (μ_{DEC}) are used to separate out the contamination of field stars from the cluster members (Gaia Collaboration et al. 2018b). The average proper motions obtained for NGC 7492 using GAIA DR2 data are $(\mu_{RA}, \mu_{DEC}) = (0.799, -2.273)$ mas/yr (Vasiliev 2019; Baumgardt et al. 2019). We cross-matched the UVIT sources with a catalog of the GAIA DR2 within a matching radius of $1.5''$. We found 424 sources in NUVB4, 322 sources in NUVB13, 67 sources in NUVB15, 42 sources in Silica and 45 sources in BaF2 filters have counterparts in the Gaia DR2 catalog. We obtained the proper motions (μ_{RA}, μ_{DEC}) and optical magnitudes (G, BP and RP bands) from the catalog and converted the G, BP and RP band magnitudes into AB-magnitudes using zero point fluxes in AB-magnitude and Vega magnitude systems given for respective filters at Spanish Virtual Observatory (SVO) filter profile service³. We estimated the mean μ_{RA} and mean μ_{DEC} as 0.799 mas/yr and -2.338 mas/yr, respectively, using Gaussian dispersion over vector-point diagram (VPD) of all the cross-matched sources. Finally, we were left with a total of 175 sources in NUVB4, 128 sources in NUVB13, 41 sources in NUVB15 and 40 sources in each Silica and BaF2 filters as cluster members.

3 COLOR-MAGNITUDE DIAGRAMS

Schiavon et al. (2012) have found a dominant blue horizontal feature in the UV CMDs for NGC 7492 using the GALEX data. We have moved a step further in studying the details about the different evolutionary stages of the cluster members in UV and UV-optical CMDs. We have plotted Silica–NUVB4 vs Silica, NUVB13–NUVB4 vs NUVB13, NUVB4–G vs NUVB4, BP–RP vs BP CMDs for all the confirmed sources in Figure 2. The stars of different evolutionary stages of the cluster were predominantly identified based upon their position in NUVB4–G vs NUVB4 and BP–RP vs BP CMDs. We found 39 BHBs, one EHB star and one variable star in FUV filters (BaF2 and Silica) and 39 BHBs, one EHB star, 4 BSs, 5 variable stars, 6 AGBs, 91 RGBs and 28 SGBs sources in NUV filters (NUVB15, NUVB13 and NUVB4). The morphology of different evolutionary stages visible in UV and UV-optical CMDs is given in the following sub-sections.

3.1 Blue Horizontal Branch Stars (BHBs)

The UV, UV-optical and optical CMDs for all the 39 BHBs are shown in Figure 2. Out of 39 BHBs, two are not having proper motion information but they are included in the list based upon their position in CMDs (light blue solid circles in Figure 2). BHBs are the hottest and brightest sources in UV, therefore, only these sources along with the lone EHB star are detected in FUV. That's why no other sources are seen in Silica–NUVB4 vs Silica CMD. Whereas in other CMDs, we see all detected sources including BHBs. For all BHBs in Silica–NUVB4 vs Silica CMD, the magnitude in Silica filter ranges from 19.10 to 20.51 mag and the Silica–NUVB4 color ranges from -0.33 to 1.03 mag (upper left panel, Figure 2).

Of the 39 BHBs of the cluster, 35 are common in the GALEX observation (Schiavon et al. 2012). We found 11 BHBs of NGC 7492 in SIMBAD, out of which 10 were reported as blue stars from the GALEX observation (Atlee & Gould 2007) and one was reported as field BHB star by Christlieb et al. (2005), which we verified to be a cluster member based upon its proper motion and position in CMDs. The early studies by Buonanno et al. (1987); Cote et al. (1991) reported a less number of BHBs as their observations were concentrated within the half light radius of the cluster. We have observed 18 BHBs out of 39 lie outside the half light radius of the cluster. The photometric details of the 39 BHBs observed with the five UVIT filters are given in Table 2.

3.2 Red Giant Branch Stars (RGBs)

The morphology of RGBs in UV-optical CMDs (Schiavon et al. 2012; Piotto et al. 2015; Subramaniam et al. 2016; Sahu et al. 2019) are different from IR/optical CMDs (Sarajedini et al. 2007; Riffel et al. 2011; Vanderbeke et al. 2014; Cohen et al. 2015). The sources which are brighter but not bluer than BHBs in IR/optical get fainter and redder in UV and UV-optical CMDs as we move towards optical to UV filters. Since the cluster is located at a large distance, the RGBs become very faint to observe in FUV bands. Therefore, we do not see the RGBs in the Silica–NUVB4 vs Silica CMD. In the NUVB13–NUVB4 vs NUVB13 CMD, we see that RGBs are distributed throughout the color range from -0.1 to 1.2 mag towards the fainter magnitudes of 22 to 23 mag. Therefore, we identified the NUV detected RGBs based upon the positions of their optical counterparts in the NUVB4–G vs NUVB4 and BP–RP vs BP CMDs (red dots in lower right panel in Figure 2), where RGBs are well separated from AGBs and SGBs. We chose to keep clean RGBs up to 19.2 mag in the BP band. We found 91 RGBs in the NUVB4 and 53 RGBs in NUVB13 down to 23.0 mag. The range of color for RGBs in NUVB4–G vs NUVB4 CMD is from 2.29 to 6.50 mag, whereas the NUVB4 magnitude ranges from 21.11 to 22.63 mag. Similarly, the value of color for the RGBs ranges from 0.32 to 0.92 mag whereas the magnitude ranges from 15.70 to 19.26 mag in BP–RP vs BP CMD. We have detected 6 AGBs in both the NUVB4 and NUVB13 filters, 28 SGBs in NUVB4 filter, 6 AGBs and 6 SGBs in NUVB13 filter. These sources are plotted on NUV–NUV, NUV-optical and optical CMDs in Figure 2. The AGBs are shown with upper solid triangles and SGBs are shown with gray lower solid triangles. We see that AGBs are clearly separated from other branch sources and are lying above the RGBs in both the NUV–NUV and NUV-optical CMDs.

3.3 Variable Stars

We cross-matched the UVIT observed sources with the catalog of variable stars provided by Clement et al. (2001); Clement (2017)⁴ for NGC 7492. We detected five variable stars (three RR Lyrae stars and two SXPhes) in NUV filters and one in both FUV and NUV filters. All these variable stars are shown with dark orange diamonds in the CMDs (Figure 2). Out of the five variable stars, two RR Lyrae stars and two SXPhes lie in the inner part of the cluster and the fifth RR Lyrae star which is observed in both NUV and FUV bands lies outside the half light radius of the cluster. Of the three RR Lyrae stars, two are situated in the instability strip (the gap between BHBs and RGBs) and the other one lies within the BHB region in all the

³ <http://svo2.cab.inta-csic.es/theory/fps/>

⁴ <http://www.astro.utoronto.ca/cclement/cat/C2305m159>

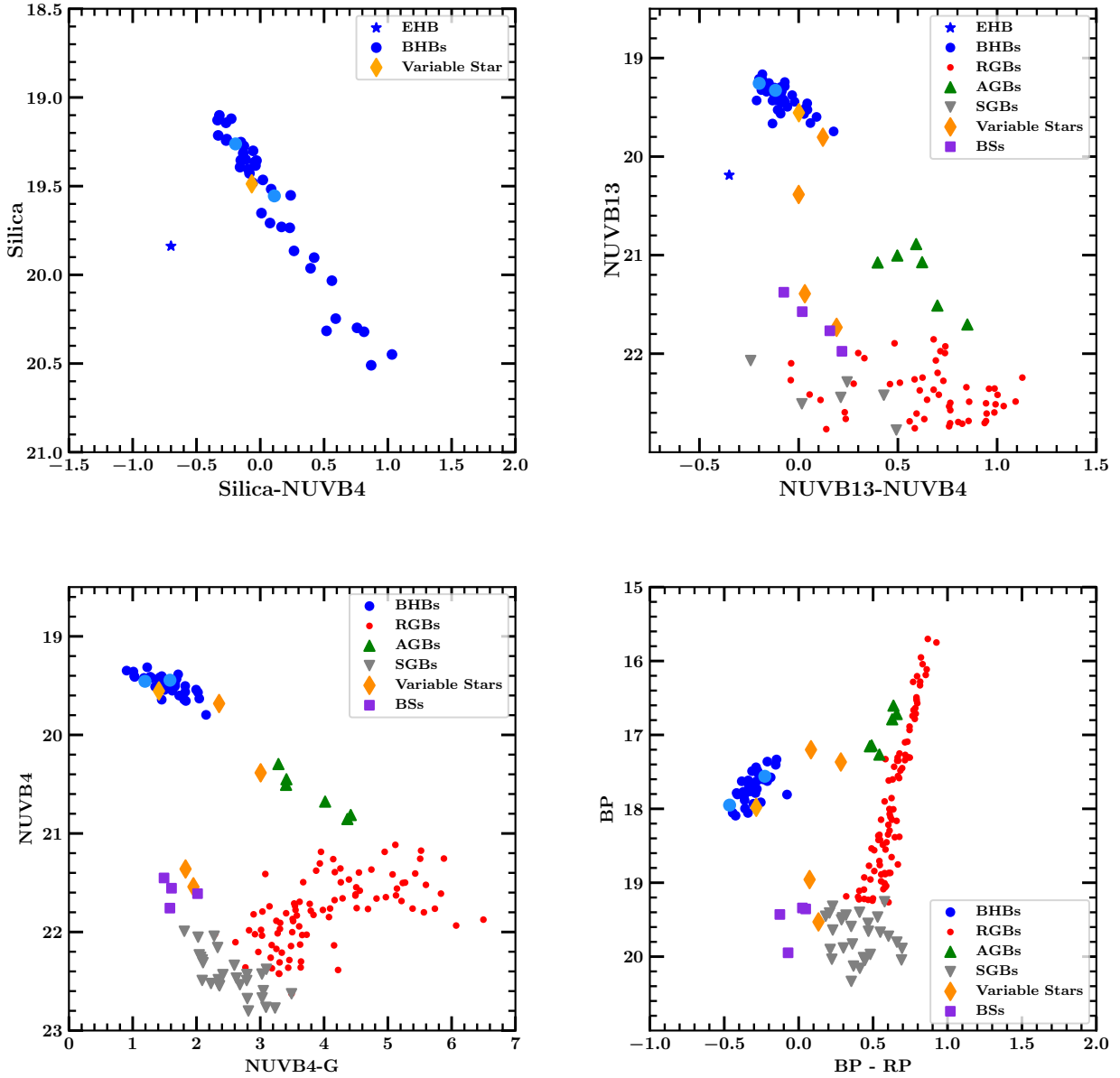


Figure 2. Silica–NUVB4 vs Silica CMD (upper left panel), NUVB13–NUVB4 vs NUVB13 CMD (upper right panel), NUVB4–G vs NUVB4 CMD (lower left panel) and BP–RP vs BP CMD (lower right panel) of the observed cluster members. EHB star is marked in blue asterisk, BHBs with Gaia proper motions are marked with blue solid points, whereas BHBs without proper motions are marked in light blue solid points. RGBs, AGBs, SGBs, variable stars and BSs are marked with red solid circles, upper solid triangles, gray lower solid triangles, and orange diamonds and violet solid squares, respectively.

CMDs (Figure 2). Since the UVIT telescope observes in photon counting mode, it is possible to study the variability and generate light curves of short period variables (Subramaniam et al. 2017).

3.4 Blue Straggler Stars (BSs)

In NUVB4–G vs NUVB4 CMD (Figure 2, lower left panel), we do not find a clear separation of the MS turn-off region from the SGBs. Hence, to avoid confusion while selecting BSs, we chose only those sources which were clearly above the MS turn-off bump. We have identified only four BSs which were bright enough in NUV filters to be separated out from MS-turnoff and SGBs in the NUV–optical

CMD. However, we do not find any BSs in FUV filters due to its lower detection limit (21.5 mag) towards the fainter sources. In this cluster, Cote et al. (1991) have reported 27 BSs with optical photometry. The radial distribution of BSs in Figure 13 of Cote et al. (1991) and Figure 13 of this paper (see section 7) show that the UVIT detected BSs are lying up to 1.5' from the center of the cluster.

Table 2. Details of 39 BHBs and one EHB star of NGC 7492 observed with UVIT filters. In the first column, we have defined a unique ID for each BHB and EHB. The extinction corrected magnitudes of UVIT and GAIA G filters are given here. The given T_{eff} with error in T_{eff} as ± 125 K of BHBs and EHB are derived from the SED fit.

ObjID	RA(J2000) hh:mm:ss.ss	DEC(J2000) dd:mm:ss.ss	BaF2±e_BaF2 ABmag	Silica±e_Silica ABmag	B15±e_B15 ABmag	B13±e_B13 ABmag	B4±e_B4 ABmag	G±e_G ABmag	PMRA mas/yr	PMDEC mas/yr	T_{eff} K
HB01	23:08:22.18	-15:36:48.65	20.05±0.18	20.27±0.24	19.83±0.38	19.60±0.03	19.40±0.03	17.847±0.003	1.090	-1.951	8,750
HB02	23:08:23.34	-15:36:49.47	20.38±0.22	19.86±0.21	20.38±0.49	19.65±0.02	19.47±0.02	17.863±0.004	0.559	-2.512	8,750
HB03	23:08:26.14	-15:36:10.97	19.95±0.23	20.18±0.23	19.45±0.32	19.56±0.03	19.54±0.03	17.813±0.003	0.568	-2.559	8,750
HB04	23:08:28.05	-15:37:01.95	21.26±0.35	19.38±0.17	20.14±0.44	19.56±0.02	19.43±0.04	17.538±0.002	1.019	-2.295	8,000
HB05	23:08:18.99	-15:35:51.23	20.15±0.20	19.22±0.13	19.30±0.30	19.42±0.03	19.43±0.03	18.045±0.002	0.481	-2.140	9,250
HB06	23:08:37.71	-15:38:56.00	19.47±0.19	19.66±0.20	19.88±0.39	19.44±0.02	19.32±0.03	17.985±0.002	0.504	-2.417	9,000
HB07	23:08:20.46	-15:37:35.75	20.21±0.22	19.18±0.20	19.56±0.34	19.43±0.02	19.36±0.03	17.890±0.002	0.801	-2.432	9,000
HB08	23:08:36.71	-15:36:35.41	19.62±0.14	19.75±0.22	18.81±0.24	19.26±0.03	19.32±0.02	17.735±0.003	0.372	-2.306	9,000
HB09	23:08:31.51	-15:36:33.18	20.13±0.22	19.17±0.12	19.37±0.31	19.31±0.02	19.39±0.03	18.019±0.002	1.135	-2.663	9,250
HB10	23:08:19.08	-15:36:34.00	19.40±0.15	19.01±0.16	18.97±0.26	19.26±0.02	19.23±0.02	18.338±0.004	0.901	-2.199	10,250
HB11	23:08:31.27	-15:37:32.95	19.45±0.22	19.40±0.24	19.57±0.34	19.36±0.02	19.30±0.02	18.127±0.003	1.217	-1.480	9,750
HB12	23:08:30.62	-15:37:10.02	19.51±0.16	19.17±0.16	19.20±0.29	19.33±0.02	19.30±0.03	18.237±0.003	0.487	-2.855	9,750
HB13	23:08:25.66	-15:37:06.65	19.69±0.18	19.69±0.22	19.36±0.31	19.28±0.02	19.27±0.03	17.664±0.002	1.309	-2.250	9,000
HB14	23:08:20.75	-15:37:19.81	20.52±0.27	19.71±0.20	19.28±0.30	19.52±0.02	19.52±0.03	17.580±0.002	0.942	-2.042	8,250
HB15	23:08:22.47	-15:36:22.64	19.88±0.19	19.44±0.25	18.91±0.25	19.41±0.02	19.53±0.02	18.179±0.003	0.733	-2.144	9,500
HB16	23:08:38.19	-15:33:30.10	20.00±0.19	19.36±0.18	19.40±0.31	19.41±0.02	19.39±0.03	17.870±0.003	1.082	-1.945	9,000
HB17	23:08:26.23	-15:38:40.55	20.05±0.21	19.39±0.20	19.38±0.31	19.51±0.03	19.38±0.02	17.938±0.003	0.647	-2.198	9,000
HB18	23:08:22.56	-15:38:25.47	20.54±0.21	19.96±0.21	19.18±0.28	19.54±0.03	19.54±0.03	17.827±0.002	0.654	-1.812	8,500
HB19	23:08:28.96	-15:36:14.96	19.98±0.26	20.52±0.33	19.89±0.40	19.44±0.02	19.43±0.02	17.92±0.002	0.283	-2.807	8,750
HB20	23:08:31.30	-15:37:01.57	19.70±0.15	19.37±0.14	19.13±0.28	19.21±0.02	19.20±0.02	18.078±0.003	0.310	-2.529	9,500
HB21	23:08:29.22	-15:35:14.88	19.73±0.147	19.33±0.18	19.06±0.27	19.35±0.02	19.33±0.03	18.026±0.002	0.521	-2.473	9,500
HB22	23:08:26.65	-15:36:07.52	19.59±0.16	19.23±0.17	19.10±0.28	19.20±0.02	19.29±0.03	18.373±0.004	1.222	-2.103	10,500
HB23	23:08:27.28	-15:37:05.99	21.32±0.41	20.12±0.31	19.40±0.31	19.65±0.02	19.68±0.04	17.638±0.003	0.631	-2.472	8,000
HB24	23:08:26.82	-15:36:34.66	20.04±0.22	19.59±0.23	19.20±0.29	19.27±0.03	19.29±0.03	17.940±0.003	1.173	-2.125	9,000
HB25	23:08:27.27	-15:37:20.24	19.77±0.19	19.77±0.26	19.32±0.30	19.30±0.02	19.32±0.02	18.114±0.003	0.569	-2.321	9,500
HB26	23:08:28.40	-15:35:46.21	19.82±0.16	20.12±0.32	19.30±0.30	19.51±0.02	19.36±0.02	17.808±0.007	0.689	-2.669	8,750
HB27	23:08:30.99	-15:37:45.53	19.58±0.119	18.90±0.14	18.90±0.25	19.16±0.02	19.25±0.03	18.435±0.003	1.676	-2.512	10,500
HB28	23:08:26.65	-15:38:06.14	20.08±0.23	19.85±0.23	19.41±0.32	19.33±0.02	19.39±0.03	17.672±0.002	0.860	-2.543	8,750
HB29	3:08:29.73	-15:35:00.16	19.94±0.20	19.64±0.24	19.19±0.27	19.32±0.02	19.35±0.02	18.034±0.003	0.392	-2.437	9,250
HB30	23:08:25.38	-15:36:39.99	20.43±0.27	19.64±0.18	19.39±0.31	19.39±0.03	19.37±0.03	17.932±0.003	0.159	-2.411	8,750
HB31	23:08:22.22	-15:36:00.59	19.58±0.21	18.93±0.14	19.31±0.30	19.33±0.02	19.32±0.02	18.244±0.003	0.678	-2.222	10,000
HB32	23:08:22.88	-15:36:50.52	21.08±0.38	20.42±0.27	18.94±0.25	19.74±0.03	19.45±0.02	17.547±0.002	1.514	-2.542	8,000
HB33	23:08:27.96	-15:36:17.76	19.76±0.19	19.70±0.21	19.72±0.37	19.36±0.02	19.38±0.03	17.938±0.002	1.082	-2.199	9,000
HB34	23:08:34.97	-15:38:21.46	20.39±0.24	19.91±0.27	19.51±0.33	19.48±0.02	19.44±0.03	17.922±0.002	0.593	-2.091	8,750
HB35	23:08:22.13	-15:36:10.09	20.13±0.19	19.43±0.21	19.44±0.32	19.43±0.03	19.38±0.02	18.150±0.003	0.632	-2.659	9,250
HB36	23:08:27.00	-15:35:48.20	20.22±0.23	19.12±0.14	19.28±0.30	19.23±0.03	19.36±0.03	18.255±0.005	-	-	9,500
HB37	23:08:26.30	-15:37:17.49	19.93±0.20	18.90±0.17	19.08±0.27	19.20±0.03	19.30±0.04	18.370±0.006	0.358	-3.855	10,000
HB38	23:08:30.95	-15:36:56.17	20.54±0.22	19.94±0.24	19.58±0.34	19.41±0.03	19.44±0.02	17.732±0.003	0.734	-2.042	8,500
HB39	23:08:25.85	-15:35:30.37	19.83±0.17	19.71±0.21	19.06±0.27	19.31±0.02	19.33±0.02	17.852±0.003	-	-	9,000
EHB01	23:08:25.10	-15:36:26.86	20.28 ± 0.20	19.84 ± 0.23	20.17 ± 0.45	20.19 ± 0.04	20.54 ± 0.05	-	-	-	29,000

4 CONSTRAINING VARIOUS PARAMETERS OF THE CLUSTER

We have cross-matched the UVIT detected sources of NGC 7492 with the catalog of ground-based observations provided by [Stetson et al. \(2019\)](#). In [Figure 3](#), we have plotted the V-I vs V CMD for all the sources obtained from the wide-field ground-based observations in gray solid circles and over-plotted the UVIT detections in magenta solid circles. The presence of stars of almost all possible stages of evolution are noticed in the ground-based observation whereas only the SGBs and the stars of later stages of evolution are seen in the UVIT observations. Various parameters of the cluster such as metallicity, age, distance, etc., are generally estimated by fitting isochrones on the turn-off region of the main-sequence (MSTOS) and on the SGBs. In [Figure 3](#), we see a sharp turn-off region along with good number of SGBs which we have used in constraining the cluster parameters.

In the following subsections, we have constrained distance to the cluster and He-abundance of BHBs using BaSTI model isochrones and zero-age horizontal branch (ZAHB) over UV, UV-optical and optical CMDs.

4.1 Distance estimation

We have generated isochrones of the updated BaSTI stellar evolution models ([Hidalgo et al. 2018](#)) with the following input parameters: $[Fe/H] = -1.8$, age = 12.0 Gyr and distance-modulus (DM) values ranging from 16.8 to 17.1. We show the over-plotted isochrones on V-I vs V CMD in [Figure 3](#). The inset plot in [Figure 3](#) shows the SGB region of the cluster. The best fitted isochrone to the SGB region is having a distance modulus 16.95 (cyan line). The isochrones get merged below the turn-off point and do not show much variation in the MS or RGB region. The isochrones at HB region also show a clear deviation at the distance modulus of 17.1. Thus, we conclude that the distance modulus of the cluster to be 16.95 ± 0.05 which is equivalent to 24.5 ± 0.5 kpc. Previously, [Figuera Jaimes et al. \(2013\)](#) have estimated the distance to the cluster using period-luminosity relation of variable stars. They found it to be 25.2 ± 1.8 kpc using SxPhes stars and 24.3 ± 0.5 kpc using RR Lyrae stars which are in agreement within error with our estimation.

4.2 Helium abundance of BHBs

The temperature of UVIT observed BHBs ranges from 8,000 K to 10,500 K (see [section 5](#)), which is suitable to see the variation of He-abundances in them ([Marino et al. 2014](#)). In [Figure 4](#), we have plotted the α -enhanced ZAHB from the updated BaSTI model for

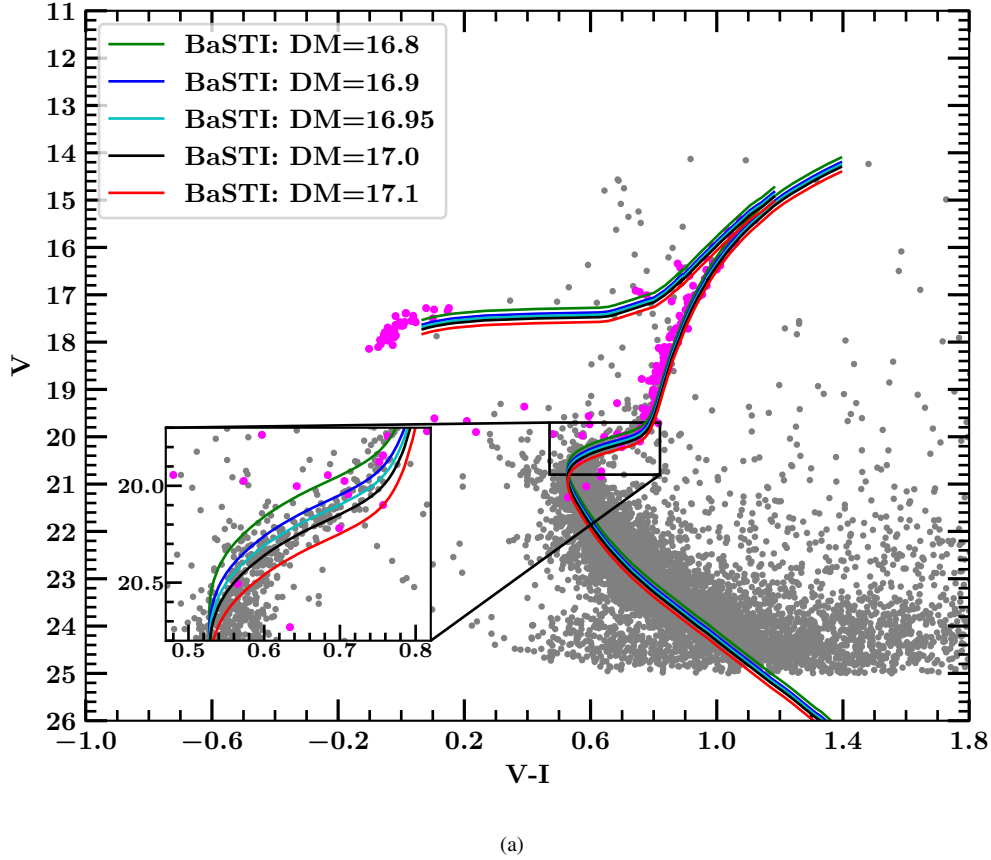


Figure 3. V-I vs V CMD of ground-based photometry of NGC 7492 provided by Stetson et al. (2019) (gray solids)). The sources cross-matched with UVIT detections are over-plotted in magenta solids. The BaSTI isochrones generated for age 12.0 Gyr and $[Fe/H] = -1.8$ have been over-plotted for various distance modulus (DM) as indicated in the legend. The inset panel shows the SGB region.

three He-abundances, $Y = 0.247, 0.300$ and 0.350 , and $[Fe/H] = -1.8$ over optical, NUV-optical and FUV-optical CMDs. We see He-abundances of BHBs, Y in the range, 0.247 to 0.350 in V-I vs V, Silica-V vs Silica, NUVB15-V vs NUVB15, and BaF2-V vs BaF2 CMDs (Figures 4a, 4e, 4d, and 4f, respectively). Similarly, it is between $Y = 0.247$ and 0.300 in NUVB13-V vs NUVB13 and NUVB4-V vs NUVB4 CMDs (Figures 4c and 4b, respectively). Marino et al. (2014); Villanova et al. (2012) and Behr (2003) have used the prominent He I line at 5875 \AA to estimate the He-content of BHBs in several GGCs. Since this line is lying within the waveband of V filter ($\lambda_{\text{eff}} = 5445 \text{ \AA}$), we also see He enhancement in BHBs of the cluster NGC 7492 (Figure 4a). The NUVB15 filter ($\lambda_{\text{eff}} = 2193 \text{ \AA}$) is heavily affected by the extinction bump ($\lambda_{\text{eff}} = 2175 \text{ \AA}$) and also the signal to noise ratio was very low due to small exposure time for BHBs observed in this filter. We do not consider this filter as a good estimator of He-content though we see a He-enrichment of 0.05 to 0.10 (Figure 4d). From the Figures 4e and 4f, it is obvious that the FUV filters are the best estimator of the He-abundances of BHBs and we see a clear variation from $Y = 0.247$ to $Y = 0.350$ in the FUV filters. However, it is very difficult to comment on the contribution of prominent He lines within the wavelength range of our FUV filters since the synthetic spectra of BHBs with He-abundance higher than $Y = 0.247$ is not available in FUV regime. Since, we have used α -enhanced plus He-normal

and also He-enhanced ZAHB, we suggest that the enhancement in metal content (or He) are definitely present in BHBs of NGC 7492.

Earlier the He-content of the cluster was estimated to be 0.23 ± 0.06 using R-parameter, which is the number ratio of BHBs to upper RGBs in B-V vs V CMD (Cote et al. 1991; Buonanno et al. 1987). While calculating the He-content, they used only 18 BHBs, 20 RGBs and 5 AGBs as their observations were concentrated within the core of the cluster. With the observation up to the tidal radius of the cluster, we have detected more number of these sources (i.e., 39 BHBs, 20 RGBs and 6 AGBs) in the cluster than previously observed. Using the number of these sources in the formulas given in Buzzoni et al. (1983), we have calculated R, and R' and hence, the corresponding He abundances as follows:

$$R = \frac{N(\text{HB})}{N(\text{RGB})} = \frac{39}{20} = 1.95 \quad (1)$$

$$R' = \frac{N(\text{HB})}{N(\text{RGB} + \text{AGB})} = \frac{39}{20 + 6} = 1.5 \quad (2)$$

$$Y = 0.380 \times \log(R) + 0.176 = 0.380 \times \log(1.95) + 0.176 = 0.286 \quad (3)$$

$$Y' = 0.457 \times \log(R') + 0.204 = 0.457 \times \log(1.5) + 0.204 = 0.284 \quad (4)$$

Using the Poisson error in the number statistics of BHBs and RGBs,

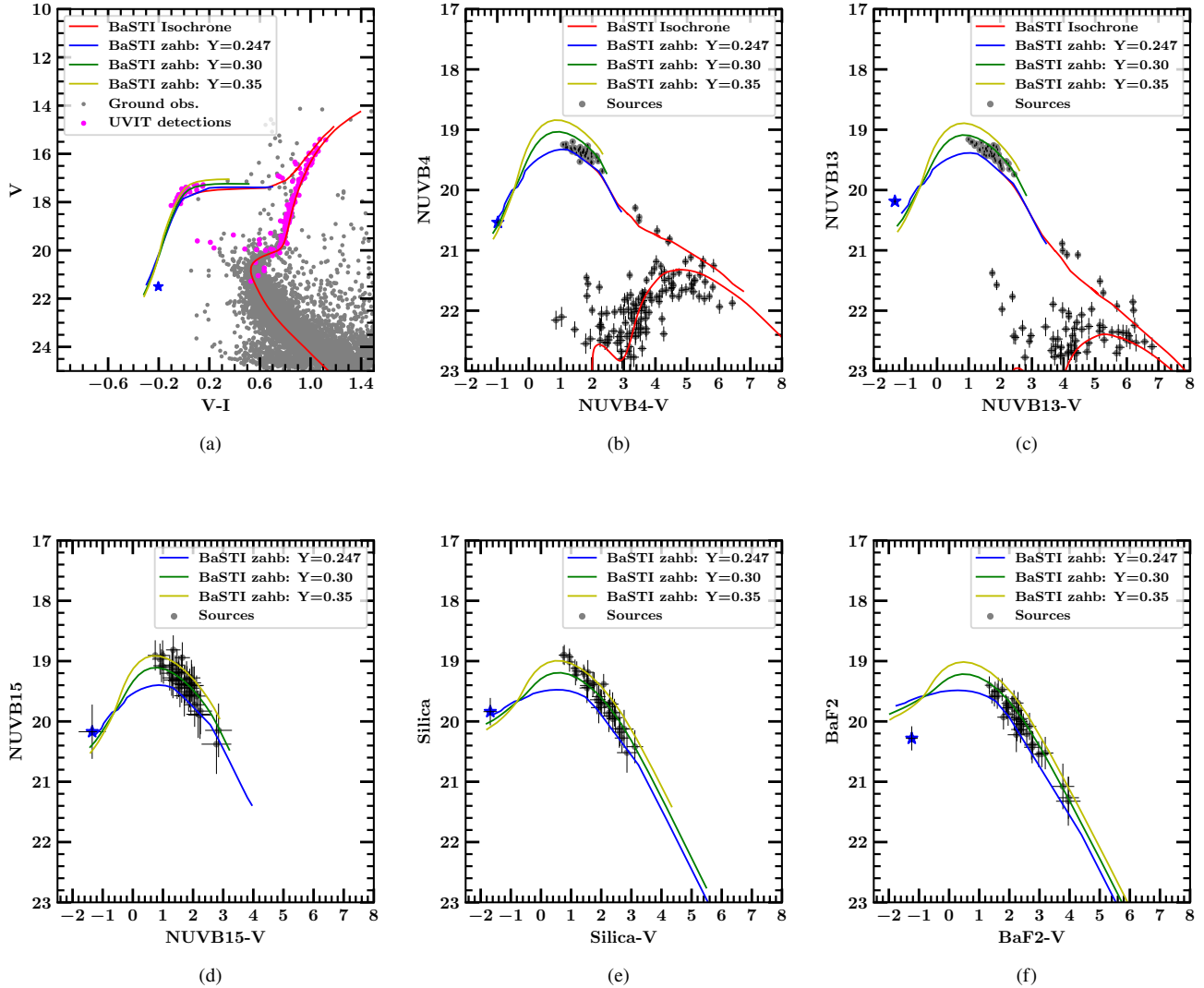


Figure 4. Optical, NUV–optical and FUV–optical CMDs of UVIT sources are shown along with BaSTI isochrones with He-abundant ZAHB for He-abundance 0.247 (blue line), 0.300 (green line) and 0.350 (yellow line). In panel (a) we have plotted the V–I vs V CMD of all the sources obtained from ground-based observations in gray solids. Cross-matched UVIT sources are overplotted in magenta solids. In panels (b), (c), (d), (e), and (f), we have plotted CMDs of UVIT filters NUVB4, NUVB13, NUVB15, Silica, and BaF2, respectively in combination with ground-based observations of V filter. The UVIT detected sources in all the CMDs are shown in black solids along with the associated error-bars. The lone EHB star is marked in blue asterisk in all the CMDs.

the estimated He-abundance of the cluster is 0.28 ± 0.05 . Hence, the He-abundance obtained from the CMDs and the R-parameters are in good agreement.

5 TEMPERATURE DISTRIBUTION OF BHBS

BHBs are very hot stars with T_{eff} ranging from 8,000 K to 30,000 K. The T_{eff} of BHBs mainly depends on the amount of mass loss during the helium flash at the RGB tip. The larger mass loss gives the lesser H-rich envelope and hence, the higher T_{eff} of BHBs and vice versa. We have estimated T_{eff} of BHBs using the Kurucz stellar atmospheric model (Castelli et al. 1997; Castelli & Kurucz 2003, hereafter Kurucz model). However, it is done by two methods; (i) using the color-temperature relation obtained from the Kurucz model and then matching the observed colors with the model gen-

erated colors for various UVIT filters (ii) using SED analysis of the observed fluxes obtained from the five UVIT filters, and the photometric fluxes obtained from the archival catalog of various filters of *GALEX*, *GAIA*, *Pan-STARRS*, *CFHT*, and *CTIO-4m* telescopes. We have described the two methods in the following subsections separately.

5.1 Temperature distribution using color-temperature relation

We have used Spanish Virtual Observatory⁵ (SVO, Bayo et al. 2008) to develop synthetic photometry for UVIT filters using the Kurucz model. For a given temperature, metallicity and surface gravity,

⁵ <http://svo2.cab.inta-csic.es/theory/newov2/syph.php>

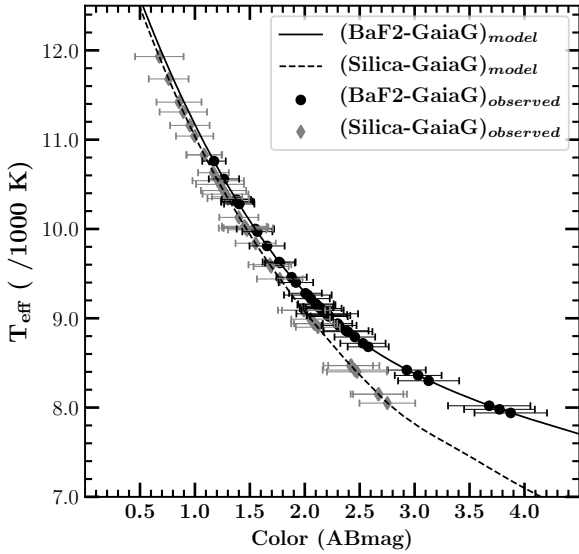


Figure 5. The color-temperature relations of Silica - GaiaG and BaF2 - GaiaG colors with their corresponding effective temperatures from the Kurucz model. The synthetic color-temperature curves of $\log(g) = 3.0$ in solid (dashed) lines are shown for BaF2 - GaiaG (Silica - GaiaG) colors. The observed colors, BaF2 - GaiaG and Silica - GaiaG are over plotted with black and gray points. The error-bars in the observed colors are the effective error obtained from the magnitude errors of both filters.

SVO produces synthetic photometric fluxes for various filters by convolving the filter responses with the Kurucz model. We generated synthetic fluxes for Silica, BaF2 and Gaia G filters adopting metallicity $[Fe/H] = -2.0$ dex (nearest grid to the cluster metallicity, $Fe/H = -1.8$), the temperature in the range from 4,000 K to 50,000 K (with a step-size of 250 K from 4,000 to 13,000 K and a step size of 1,000 K above that) and the value of $\log(g) = 3.0$. We interpolated the model generated effective temperatures with a step size of 10 K using cubic interpolation to get a closer color match for the observed BHBs. In Figure 5, we have plotted the model generated color - temperature curves separately for BaF2 - GaiaG and Silica - GaiaG colors and overlaid on the observed colors of all BHBs. We got a range of T_{eff} from 8,000 K to 12,000 K using Silica - GaiaG colors and 8,000 K to 10,750 K using BaF2 - GaiaG colors for all the BHBs. We found that the observed Silica magnitudes for most of the BHBs are brighter than the corresponding BaF2 magnitudes. This difference in observed magnitudes gives rise to a shifting of Silica - GaiaG color relative to the BaF2 - GaiaG color ($\Delta_c > 0.5$ mag) as seen in Figure 5. Again, we see from the figure that there is not much difference between the two synthetic colors at higher T_{eff} ($> 9,000$ K, color ≤ 2.0 mag). Therefore, T_{eff} we obtained from Silica - GaiaG colors is slightly higher than the values obtained from the BaF2 - GaiaG colors.

5.2 Temperature distribution from SEDs

The effective temperature of a source depends upon its SED through all the wavelength range. To study SEDs of the detected BHBs, we used UVIT, GALEX, GAIA, PanSTARSS, ground-based UBVRI photometry from Stetson et al. (2019) catalog, and ground-based g and r band photometry from Muñoz et al. (2018). The filter de-

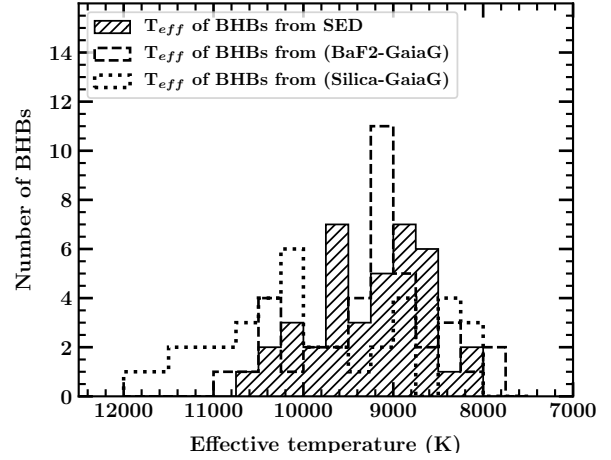


Figure 6. Histogram distributions of effective temperatures of BHBs derived from both SED fitting, and BaF2 - GaiaG and Silica - GaiaG color temperature relations.

tails, wavelength range, and date of observation are given in Table 3. When compared the number of BHBs detected in UVIT with GALEX we found some discrepancy. Out of 39 UVIT detections of BHBs, two were not reported in Schiavon et al. (2012). Another four BHBs of UVIT detection are reported as two in GALEX observation as they were not resolved in GALEX due to its poor resolution. Ultimately, out of 39 BHBs we have used the best available photometric data of 33 BHBs from GALEX observations. Thus, we have used the photometric observations in 22 filters for 33 BHBs and in 20 filters for the rest of the 6 BHBs from FUV to NIR.

We used the virtual observatory of SED analyzer (VOSA, Bayo et al. 2008) to fit the observed photometric fluxes with the Kurucz model, ATLAS9 (Castelli et al. 1997; Castelli & Kurucz 2003). VOSA includes various grids (spectra) of Kurucz atmosphere models. We have adopted the Kurucz model grids of metallicity -2.0 and -1.5 (nearest grids to the cluster metallicity, $Fe/H = -1.8$) to fit the observed flux of BHBs with the Kurucz model. We have used chi-square minimisation technique to fit the observed flux with the model at the corresponding effective wavelengths of photometric filters. We find that the temperature ranges from 8,000 K to 10,500 K using SEDs fit of the BHBs.

5.3 Comparison of effective temperatures

In Figure 6, we have shown the distributions of T_{eff} of BHBs derived from both the SEDs fit and color-temperature relations. We see that the BaF2 - GaiaG effective temperature ($T_{\text{eff}}^{\text{BaF2-GaiaG}}$) is closer to the SED effective temperature ($T_{\text{eff}}^{\text{SED}}$) than the Silica - GaiaG effective temperature ($T_{\text{eff}}^{\text{Silica-GaiaG}}$).

We have plotted $T_{\text{eff}}^{\text{SED}} - T_{\text{eff}}^{\text{Silica-V}}$ and $T_{\text{eff}}^{\text{SED}} - T_{\text{eff}}^{\text{BaF2-V}}$ against $T_{\text{eff}}^{\text{SED}}$ with solid circles in the top left and right panels of Figure 7. We have shown the Silica - V vs Silica and BaF2 - V vs BaF2 CMDs, in the bottom left and right panels, respectively, along with the ZAHB for He-abundances $Y = 0.247, 0.300$ and 0.350 . In the Silica filter (left top and bottom panels), the BHBs which are lying in between isochrones for $Y = 0.247$ and $Y = 0.300$ show ΔT of ± 500 K. The BHBs observed at He-abundance close to $Y = 0.350$ have deviation in T_{eff} of more than 1,000 K from $T_{\text{eff}}^{\text{SED}}$. Some of

Table 3. List of the Telescopes and their filters used in the SEDs fit.

Telescope	Filters	Wavelength range	Date of Observation	Reference
UVIT	BaF2, Silica, NUVB15, NUVB13, NUVB4	1350-2800 Å	2016 Oct 19	This paper
GALEX	FUV, NUV	1350-3000 Å	2005 Aug 26	Schiavon et al. (2012)
GAIA	G, BP, RP	3300-10600 Å	-	Gaia Collaboration et al. (2018a)
PAN-STARRS	g, r, i, z, y	3900-10800 Å	2012 June 22	Chambers et al. (2016)
CTIO-4m	U, B, V, R, I	3000-11800 Å	2009 Nov 23	Stetson et al. (2019)
CFHT	g, r	3900-7200 Å	2009 Nov	Muñoz et al. (2018)

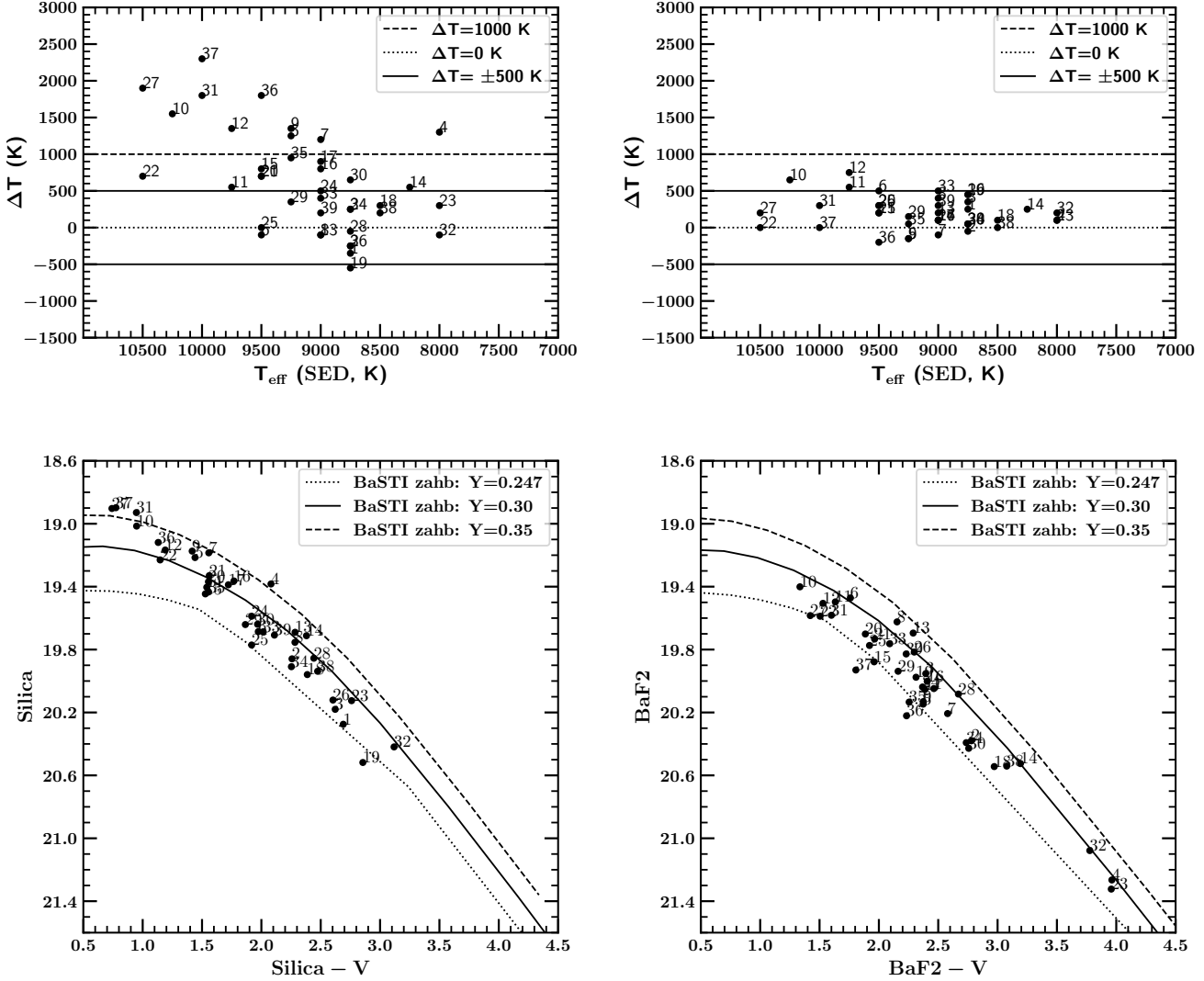


Figure 7. The top left and right panels represent plots of $T_{\text{eff}}^{\text{SED}}$ vs ΔT ($T_{\text{eff}}^{\text{SED}} - T_{\text{eff}}^{\text{Silica-V}}$) and $T_{\text{eff}}^{\text{SED}}$ vs ΔT ($T_{\text{eff}}^{\text{SED}} - T_{\text{eff}}^{\text{BaF2-V}}$), respectively, with each horizontal line showing a particular temperature difference as indicated in the legends. The black solid circles are the observed BHBs and the reference numbers are the ObjID of BHBs given in Table 2. The bottom panels are Silica-V vs Silica (left) and BaF2-V vs BaF2 (right) CMDs. The BaSTI ZAHB for $Y = 0.247$, 0.30 and 0.350 are shown by dotted, solid, and dashed lines, respectively.

the BHBs, e.g., HB37, HB27, and HB31 show a deviation of T_{eff} more than 1,500 K from the $T_{\text{eff}}^{\text{SED}}$ as they are lying above $Y = 0.350$ track in Silica-V vs Silica CMD. However, with BaF2 filter (right and bottom top panels) we find an overall ΔT of ± 500 K and He-abundance of $Y = 0.247$ to 0.300 for all the observed BHBs.

A difference of 500 K (ΔT) between T_{eff} obtained from the color-temperature relation of *HST* filters and T_{eff} obtained from

spectroscopic observation of BHBs was found by Lagioia et al. (2015). A similar comparison of BHBs of NGC 288 was done with ΔT up to 1000 K using UVIT FUV-optical color-temperature relation by (Sahu et al. 2019). We found a variation of $\Delta T = \pm 500$ K in between $T_{\text{eff}}^{\text{BaF2-V}}$ ($T_{\text{eff}}^{\text{BaF2-GaiaG}}$) and $T_{\text{eff}}^{\text{SED}}$ of the observed BHBs which is in good agreement with the Lagioia et al. (2015) and Sahu et al. (2019) color-temperature estimations. However, we find a devi-

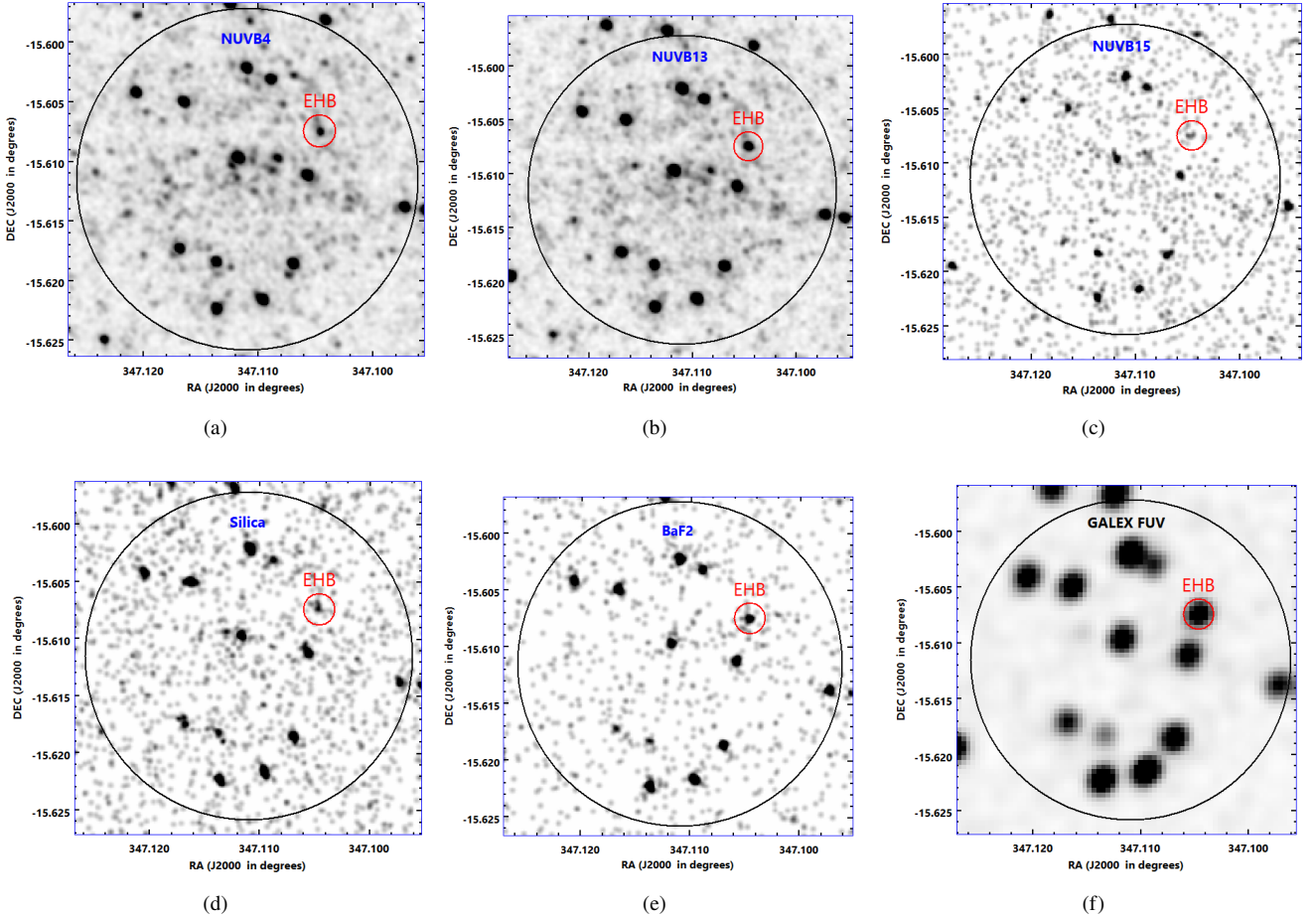


Figure 8. EHB star observed in different UVIT filters. The filter name is given in blue color on the image and the newly detected EHB star is encircled in a red circle. The black circle shows the core-radius of the cluster. We have also shown the *GALEX* FUV observation of the image in Figure (f).

ation of ΔT more than 1000 K between $T_{\text{eff}}^{\text{Silica-V}}$ ($T_{\text{eff}}^{\text{Silica-GaiaG}}$) and T_{SED} due to the larger sensitivity of Silica magnitudes towards the chemical composition (He, and α - enhancements) than the effective temperature of the BHBs.

6 EXTREME HORIZONTAL BRANCH (EHB) STAR AT THE CENTER OF THE CLUSTER

EHBs are visible as faint blue objects in optical filters and occupy the sub-dwarf (sdB/OB) region in the optical CMDs (Heber 1987). However, they are very bright in FUV filters due to their high temperature and represent the hot-flashers in UV CMDs (Dalelessandro et al. 2011). The EHBs are formed mainly due to the severe mass-loss of the outer shell of the star in their RGB phase resulting in a very thin H-envelope and a He-core of around $0.5 M_{\odot}$. The EHBs evolve towards the white dwarf phases without climbing up towards the AGB and post-AGB phases post its core-helium exhaustion. Consequently, they appear in the region with high temperature and luminosity (UV bright region) which is often known as AGB-manque region (Greggio & Renzini 1990; Dorman et al. 1993).

In the core of the cluster, we found one UV bright source at a distance of $25.48''$ from the cluster-center. This source was free from any contamination of other cluster members in all the FUV and

NUV filters (encircled with a red circle in Figure 8). When we cross-matched our UVIT sources with the deeper optical photometry from ground-based observations (Stetson et al. 2019), we identified the source as EHB star in all the UV-optical CMDs (blue asterisk in Figures 2 and 4). The UV photometric magnitude of the EHB star ranges from 19.86 mag to 20.54 mag in FUV and NUV filters. Its position and the magnitude in each UV filter are given in Table 2. This source also appears very bright in the *GALEX* FUV image (Figure 8f) and is shown in the *GALEX* FUV – NUV vs FUV CMD at the position of 0.0 mag in color with FUV magnitude of 20.3 by Schiavon et al. (2012). However, they did not discuss much about the source in their paper.

We fit the SED of the EHB star using 14 filters from UV to NIR bands to extract T_{eff} , L/L_{\odot} , and radius of the source. Again, we used VOSA SVO SED analyzer to fit the photometric fluxes to the Kurucz model synthetic fluxes for the source considering metallicity between -2.0 and -1.5 , $\log g = 5.0$, $E(B - V) = 0.04$ and distance $d = 24.5 \pm 0.5$ kpc. The SED-fit of the EHB star is shown in the upper panel of Figure 9. The coloured diamond symbols represent the observed fluxes at the effective wavelengths of the filters whereas the black solids represent the respective model fluxes. The solid line is the best fitted synthetic spectra obtained from the Kurucz model. The lower panel shows the fractional deviation of the observed flux from the model flux and indicated as residual $[(F_{\text{obs}} - F_{\text{mod}})/F_{\text{mod}}]$. The T_{eff} and bolometric luminosity of the

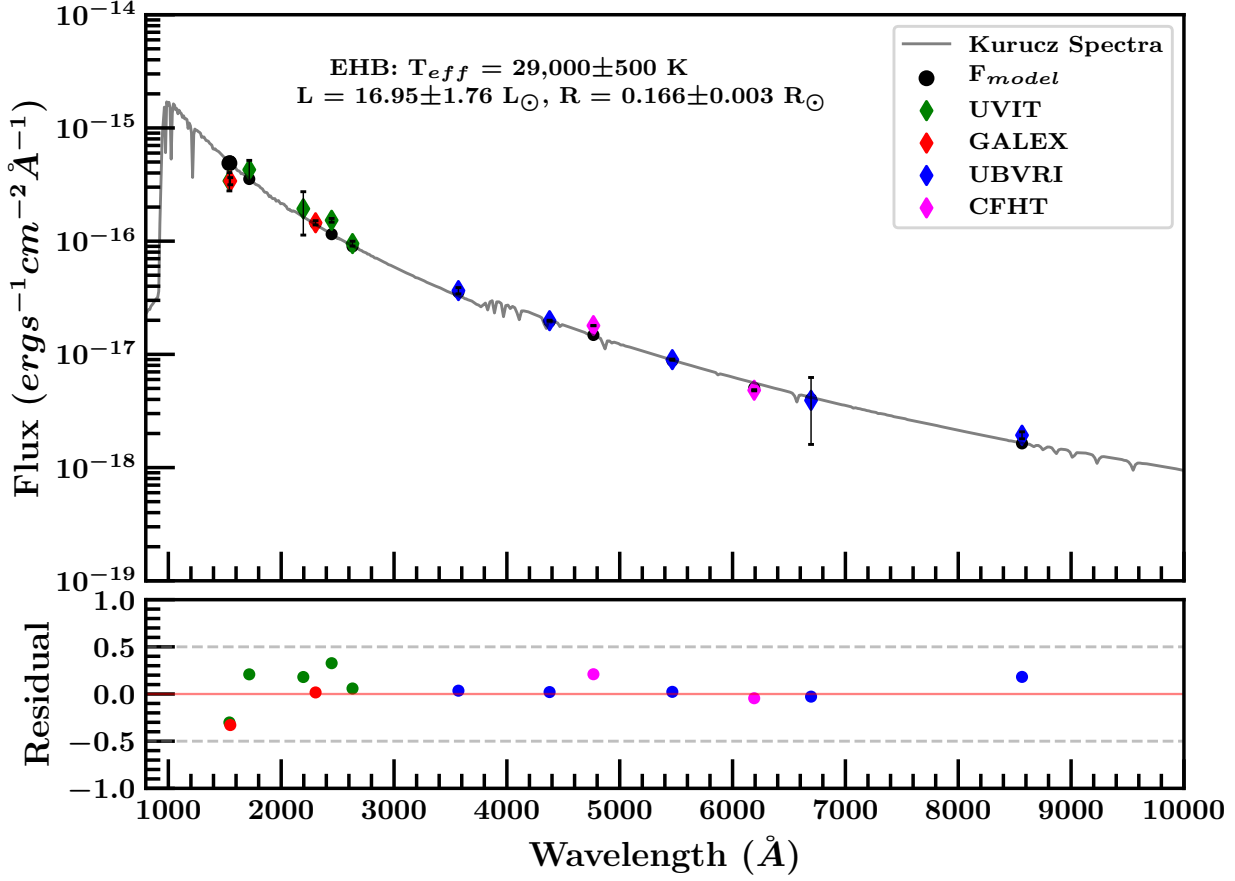


Figure 9. The SED fit of EHB star using the Kurucz model shown in upper panel. The bottom panel shows the residue (deviation) of the observed fluxes from the Kurucz model flux.

Table 4. Various physical parameters derived from the SED fit and evolutionary tracks of the EHB source. The T_{eff} , luminosity and radius are derived from the SED fit and $\log g$, mass of the source are derived from evolutionary tracks of [Dorman et al. \(1993\)](#).

ID	RA(J2000) hh:mm:ss.ss	DEC(J2000) hh:mm:ss.ss	$\chi^2_{r, \text{sed}}$	T_{eff} K	Luminosity L_{\odot}	Radius R_{\odot}	$\log(g)$	M_{EHB} M_{\odot}	M_{core} M_{\odot}	M_{envelope} M_{\odot}
EHB01	23:08:25.10	-15:36:26.86	12.66	$29,000 \pm 500$	16.95 ± 1.76	0.166 ± 0.003	5.72	0.498	0.495	0.003

EHB star were calculated from the slope of the best fitted spectrum. The radius of the EHB star was calculated from the scaling relation $\left(\frac{R}{d}\right)^2$ used in the SED fit, where R is the radius of the source and d is the distance. The derived parameters are listed in [Table 4](#).

[Dorman et al. \(1993\)](#) have provided the post-HB evolutionary tracks for $[Fe/H] = -1.48$ and -2.26 for metal poor stars. Since the derived T_{eff} of the observed EHB star is 29,000 K, we see that the post-HB evolutionary track with $[Fe/H] = -2.26$ and M_{HB} of $0.498 M_{\odot}$ is lying close to the observed EHB star as seen in [Figure 10](#). Considering this track as the actual evolutionary track of the observed EHB star, we have also derived its surface gravity, core mass and envelope mass which are given in [Table 4](#).

7 DISTRIBUTION OF SOURCES IN THE CLUSTER

We have classified all the sources of NGC 7492 which have been detected in various filters of UVIT. Interestingly, only the EHB star, BHBs and one RR Lyrae star have been detected in FUV. We have shown the UVIT detected BHBs with the assigned unique IDs ([Table 2](#)) on the inverted image of the NUVB4 filter (left panel, [Figure 11](#)). We see from [Figure 11](#) that 21 of the BHBs are located within the half-light radius of the cluster, and remaining 18 are lying outside the half-light radius. We have over-plotted the *GALEX* counterparts of BHBs in red circles and the newly identified BHBs (ObjID: HB03, HB23, HB32 and HB37) in UVIT in blue circles. Only 11 BHBs of our sample are available in SIMBAD ([Christlieb et al. 2005](#); [Atlee & Gould 2007](#)) which are denoted by green circles. The BHB, “HB08” in the figure was identified as a field member by [Christlieb et al. \(2005\)](#). However, the proper motion values, $\mu_{\text{RA}} = 0.372$ mas/yr and $\mu_{\text{DEC}} = -2.306$ mas/yr, support

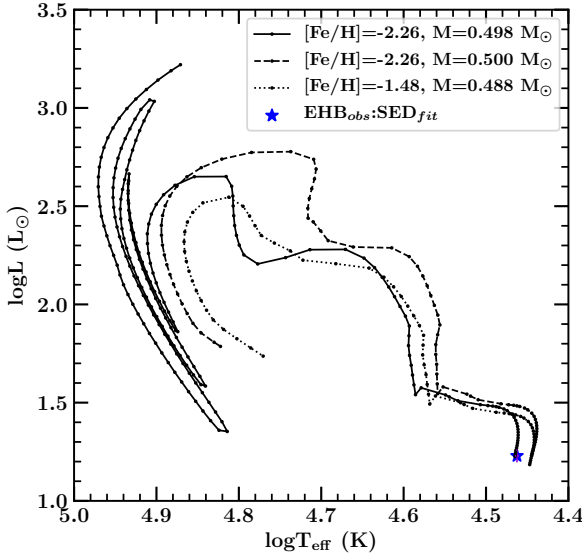


Figure 10. Post-HB evolutionary tracks of the EHB star. The evolutionary tracks with solid and dashed lines are shown for metallicity -2.26 and masses $0.498 M_{\odot}$ and $0.500 M_{\odot}$, respectively. The dotted line is the evolutionary track of metallicity -1.48 and mass $0.488 M_{\odot}$. The Blue asterisk is the position of the newly identified EHB star where $\log T_{\text{eff}}$ and $\log L$ obtained from SED fit of the EHB.

its candidature as a cluster member in our analysis. All the UVIT detected BHBs are also present in the larger FoV optical band surveys for this cluster. We have shown the temperature distribution of all BHBs in the right panel of Figure 11. The T_{eff} scale is indicated in a vertical color bar. The BHBs have a maximum spread up to $2'$ from the cluster center but the distribution of T_{eff} do not show any systematic variation. We have listed the derived temperature and the photometric magnitudes of the UVIT filters of each BHB in Table 2.

We have shown the radial distribution of all the detected sources in Figure 12. We see that almost 50% of the sources are within 10 pc (approximately up to the half-light radius of $1.15'$) of the cluster. All the BHBs are distributed up to 40 pc from the cluster center. About 80% of the RGBs are distributed within 20 pc from the center of the cluster and a tail of 5% RGBs contribute to the outer part of the cluster. Carballo-Bello et al. (2012) have shown that this cluster shows a steep density profile and extends the cluster density profile beyond the king's radius of the cluster ($R_t = 8.3'$, Harris 2010). As seen in Figure 12, the presence of RGBs in the outer region of the cluster beyond $8.3'$ supports the optical observations of Carballo-Bello et al. (2012).

Figure 13 shows the UV (NUVB4 filter) and optical (GaiaG filter) magnitude distributions of the sources over distance from the cluster center. As seen from the figure, BHBs are completely distinguished and there is a clear gap between the brightness of BHBs and RGBs + SGB populations in the UV filter (upper panel, Figure 13). However, in the optical filter (lower panel, Figure 13), all the sources are uniformly distributed at the core of the cluster. This signifies the ability of UV filters to separate out hot sources from the cooler ones. The RR Lyrae stars are lying in the gap between RGBs and BHBs in the UV magnitude distribution. This gap infers the absence of any red-HB (RHB) sources in the cluster (as suggested by Buonanno et al. 1987). The BSs are relatively

brighter than the SGBs in UV. Thus, we can infer that there are separate magnitude layers of each evolutionary stages which are hotter than RGBs and SGBs in UV photometry. In the NUV filters (NUVB13 and NUVB4), although we tried to detect the fainter sources up to 23 mag, we could find only those sources which were brighter than MS.

8 CONCLUSIONS

We have presented a detailed UV photometric analysis for the cluster NGC 7492 with five filters of UVIT. We found 176 sources in NUV and 41 sources in FUV as cluster members and classified them into EHB, BHBs, RGBs, SGBs, variable stars and BSs based upon their positions in UV – optical and optical CMDs. The sources, EHB, BHBs and one RR Lyrae star were detected in multi-band UVIT FUV and NUV filters, whereas sources above MS turn-off were detected only with NUV (NUVB13 and NUVB4) filters.

The updated BaSTI isochrones and ZAHB, generated using the available cluster parameters, are compared with the observed UV – optical CMDs. The stellar evolution track with metallicity $[Fe/H] = -1.8$, age = 12 Gyrs and a distance modulus of 16.95 ± 0.05 is fitting well with the observed optical CMDs. The He-abundances of the BHBs of the cluster are estimated using α -enhanced ZAHB from BaSTI model for various He-abundances on the UV–optical CMDs and also from the R-parameters. The He-abundance value obtained from CMDs is varying from 0.247 to 0.350 whereas R-parameter gives a value of 0.28 ± 0.05 .

We provide a catalog of BHBs along with their effective temperature and UV magnitudes in UVIT filters which will help in improving stellar evolution models and further constrain the structure of the Galaxy. The effective temperatures of all the BHBs were derived using color-temperature relation and SED fitting. The effective temperatures of all the BHBs obtained from both the methods are ranging from 8,000 K to 10,500 K with a deviation of 500 - 1,000 K from each other. Again, the effective temperature derived from the color-temperature relation of BaF2 filter differs a bit from the Silica filter due to the relative shifting of magnitudes between the filters. However, we do not find any systematic pattern in the temperature distribution of the BHBs.

We have identified one EHB star at the cluster-core at a distance of $25.48''$ from the center of the cluster. From the SED fitting we estimated its effective temperature, luminosity and radius to be $29,000 \pm 500$ K, $16.95 \pm 1.76 L_{\odot}$, and $0.166 \pm 0.003 R_{\odot}$, respectively. The post-HB evolutionary tracks from Dorman et al. (1993) are used to estimate surface gravity and mass of the star at ZAHB phase. The $\log g$ of the EHB star is 5.72 whereas its total mass is $0.498 M_{\odot}$, with core-mass $0.495 M_{\odot}$ and a very thin envelope of mass $0.003 M_{\odot}$.

The BHBs in the cluster are distributed uniformly up to 40 pc from the center of the cluster. The uniform distribution of BHBs and their temperature beyond the half-light radius up to $2'$ from the cluster center supports the dynamics of low density clusters. We find that RGBs are distributed up to the tidal radius of the cluster except one which lies outside the tidal radius suggesting the extension of tidal tails. The hot BHBs are brighter and are clearly distinguished in UV filters whereas they are mixed with the uniform distribution of RGB stars in optical filters.

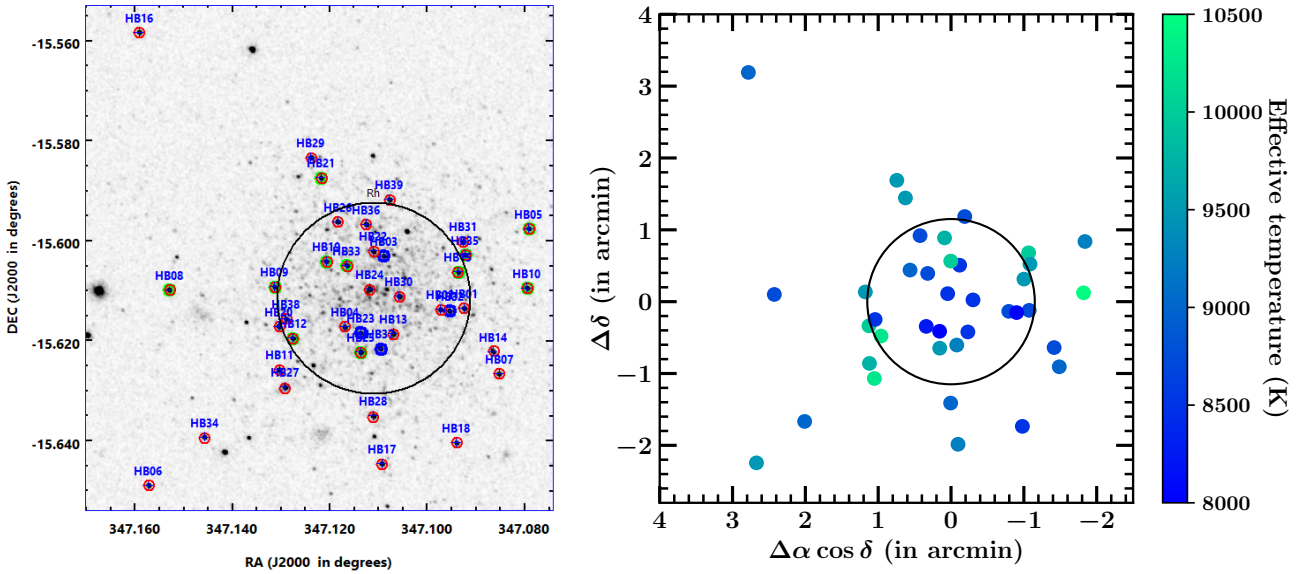


Figure 11. *left panel:* UVIT detections of 39 BHBs are overlaid on the inverted image of NUVB4 filter. We have also over-plotted the *GALEX* counterpart BHBs in red circles, the newly identified BHBs in UVIT in blue circles and the 11 available BHBs in SIMBAD are over-plotted in green circles. The half light radius ($R_h = 1.15'$) is shown in a black circle. *right panel:* The spatial distribution of BHBs at the cluster core on a 2D projection from the cluster center. X-axis is the distance from the cluster center in RA and Y-axis is the distance from the cluster center in DEC. The black circle denotes the half-light radius of the cluster. The color-bar shows the temperature distribution of the sources.

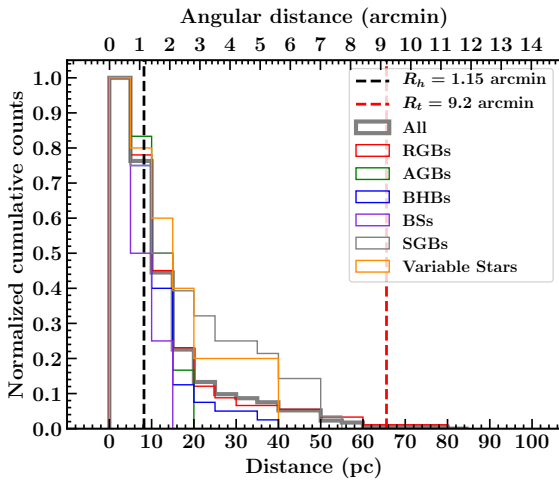


Figure 12. Cumulative radial distribution of all the stellar populations is shown here. The angular distance from the cluster center was converted into the radial distance using a distance-scale of 24.5 kpc. The sources were counted with a bin-size of 5 pc and an inverse normalized cumulative distribution is plotted here. The black dashed line is the half-light radius (R_h) and the red dashed line is the tidal-radius (R_t) of the cluster. We can see that all the sources (thick gray line) are within the tidal radius of the cluster ($R_t=9.2'$, Carballo-Bello et al. 2012), 60% of the BHBs are lying within the half-light radius of the cluster (blue line) and BSs are distributed up to 20 pc from the cluster center.

ACKNOWLEDGEMENTS

We would like to thank the anonymous referee for his/her valuable suggestions and comments. We would also like to thank Prof. Santi Cassisi, INAF - Osservatorio Astronomico d'Abruzzo: Teramo,

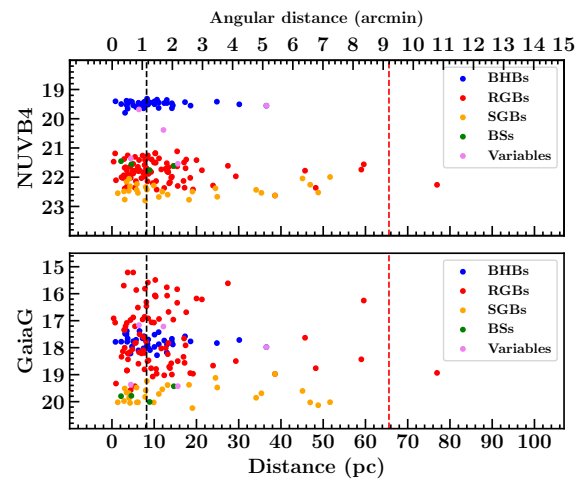


Figure 13. Magnitude distribution over distance from the cluster center of all the stellar populations observed with UVIT filters. The upper panel shows the distribution of sources and their magnitudes observed in the NUVB4 filter and the lower panel shows the distribution of GaiaG magnitudes of their optical counterparts. The black dashed line is the half-light radius (R_h) and the red dashed line is the tidal-radius (R_t) of the cluster.

Abruzzo, Italy, for providing the He-enhanced BaSTI isochrones and ZAHB of UVIT filters early in advance and also for his valuable suggestions and discussions on the He-enhancement of BHBs of the cluster. We would like to thank Dr. Snehalata Sahu of Indian Institute of Astrophysics, Bangalore for fruitful discussions with her on UVIT data reduction. RK would like to acknowledge CSIR Research Fellowship (JRF) Grant No. 09/983(0034)/2019-EMR-1 for the financial support. ACP would like to acknowledge the support by Indian Space Research Organization, Department of Space, Govern-

ment of India (ISRO RESPOND project No.ISRO/RES/2/409/17-18). AM thanks DST-INSPIRE (IF150845) for the funding. ACP thanks Inter University centre for Astronomy and Astrophysics (IUCAA), Pune, India for providing facilities to carry out his work. DKO acknowledges the support of the Department of Atomic Energy, Government of India, under Project Identification No. RTI 4002. This publication uses the data from the *AstroSat* mission of the Indian Space Research Organisation (ISRO), archived at the Indian Space Science Data Center (ISSDC). The UVIT data used here was processed by the Payload Operations Centre at IIA. The UVIT is built in collaboration between IIA, IUCAA, TIFR, ISRO and CSA.

DATA AVAILABILITY

The data underlying this article will be shared on reasonable request to the corresponding author.

REFERENCES

- Ambika S., Parthasarathy M., Aoki W., Fujii T., Nakada Y., Ita Y., Izumiura H., 2004, *A&A*, **417**, 293
- Arakelyan N. R., Pilipenko S. V., Libeskind N. I., 2018, *MNRAS*, **481**, 918
- Atlee D. W., Gould A., 2007, *ApJ*, **664**, 53
- Barnes S. A., 1968, *AJ*, **73**, 579
- Baumgardt H., Hilker M., Sollima A., Bellini A., 2019, *MNRAS*, **482**, 5138
- Bayo A., Rodrigo C., Barrado Y Navascués D., Solano E., Gutiérrez R., Morales-Calderón M., Allard F., 2008, *A&A*, **492**, 277
- Behr B. B., 2003, *ApJS*, **149**, 67
- Bond H. E., Alves D. R., 2001, *Post-AGB Stars in Globular Clusters and Galactic Halos*. Springer Netherlands, Dordrecht, pp 77–82, doi:10.1007/978-94-015-9688-6_11
- Buonanno R., Corsi C. E., Ferraro F., Fusi Pecci F., 1987, *A&AS*, **67**, 327
- Bustos Fierro I. H., Calderón J. H., 2019, *MNRAS*, **488**, 3024
- Buzzoni A., Pecci F. F., Buonanno R., Corsi C. E., 1983, *A&A*, **128**, 94
- Carballo-Bello J. A., Gieles M., Sollima A., Koposov S., Martínez-Delgado D., Peñarrubia J., 2012, *MNRAS*, **419**, 14
- Carballo-Bello J. A., Sollima A., Martínez-Delgado D., Pila-Díez B., Leaman R., Fliri J., Muñoz R. R., Corral-Santana J. M., 2014, *MNRAS*, **445**, 2971
- Carballo-Bello J. A., et al., 2018, *MNRAS*, **474**, 4766
- Cardelli J. A., Clayton G. C., Mathis J. S., 1989, *ApJ*, **345**, 245
- Castelli F., Kurucz R. L., 2003, in Piskunov N., Weiss W. W., Gray D. F., eds, *IAU Symposium Vol. 210, Modelling of Stellar Atmospheres*. p. A20 (arXiv:astro-ph/0405087)
- Castelli F., Gratton R. G., Kurucz R. L., 1997, *A&A*, **318**, 841
- Chambers K. C., et al., 2016, arXiv e-prints, p. arXiv:1612.05560
- Christlieb N., Beers T. C., Thom C., Wilhelm R., Rossi S., Flynn C., Wisotzki L., Reimers D., 2005, *A&A*, **431**, 143
- Clement C., 2017, in *European Physical Journal Web of Conferences*. p. 01021, doi:10.1051/epjconf/201715201021
- Clement C. M., et al., 2001, *AJ*, **122**, 2587
- Cohen J. G., Melendez J., 2005, *AJ*, **129**, 1607
- Cohen R. E., Hempel M., Mauro F., Geisler D., Alonso-García J., Kinemuchi K., 2015, *AJ*, **150**, 176
- Cote P., Richer H. B., Fahlman G. G., 1991, *AJ*, **102**, 1358
- Dallessandro E., Salaris M., Ferraro F. R., Cassisi S., Lanzoni B., Rood R. T., Fusi Pecci F., Sabbi E., 2011, *MNRAS*, **410**, 694
- Dallessandro E., Schiavon R. P., Rood R. T., Ferraro F. R., Sohn S. T., Lanzoni B., O’Connell R. W., 2012, *AJ*, **144**, 126
- Dallessandro E., Salaris M., Ferraro F. R., Mucciarelli A., Cassisi S., 2013, *MNRAS*, **430**, 459
- Dorman B., Rood R. T., O’Connell R. W., 1993, *ApJ*, **419**, 596
- Ferraro F. R., 2003, *Memorie della Societa Astronomica Italiana Supplementi*, **3**, 80
- Figuera Jaimes R., Arellano Ferro A., Bramich D. M., Giridhar S., Kuppuswamy K., 2013, *AAP*, **556**, A20
- Forbes D. A., Bridges T., 2010, *MNRAS*, **404**, 1203
- Freeman K. C., Norris J., 1981, *ARA&A*, **19**, 319
- Gaia Collaboration et al., 2018a, *A&A*, **616**, A1
- Gaia Collaboration et al., 2018b, *A&A*, **616**, A12
- Green G. M., Schlafly E., Zucker C., Speagle J. S., Finkbeiner D., 2019, *ApJ*, **887**, 93
- Greggio L., Renzini A., 1990, *ApJ*, **364**, 35
- Harris W. E., 2010, arXiv e-prints,
- Harris W. E., Racine R., 1979, *ARA&A*, **17**, 241
- Harris H. C., Nemec J. M., Hesser J. E., 1983, *PASP*, **95**, 256
- Heber U., 1987, in Philip A. G. D., Hayes D. S., Liebert J. W., eds, *IAU Colloq. 95: Second Conference on Faint Blue Stars*. pp 79–88
- Hidalgo S. L., et al., 2018, *ApJ*, **856**, 125
- Jain R., Vig S., Ghosh S. K., 2019, *MNRAS*, **485**, 2877
- Jasniewicz G., Parthasarathy M., 2009, in Richtler T., Larsen S., eds, *Globular Clusters - Guides to Galaxies*. Springer Berlin Heidelberg, Berlin, Heidelberg, pp 35–36, doi:10.1007/978-3-540-76961-3_10
- Jasniewicz G., de Laverny P., Parthasarathy M., Lèbre A., Thévenin F., 2004, *A&A*, **423**, 353
- Keller S. C., Mackey D., Da Costa G. S., 2012, *ApJ*, **744**, 57
- Kruijssen J. M. D., Pfeffer J. L., Reina-Campos M., Crain R. A., Bastian N., 2019, *MNRAS*, **486**, 3180
- Kumar A., Ghosh S. K., et al. 2012a, in *Space Telescopes and Instrumentation 2012: Ultraviolet to Gamma Ray*. p. 84431N (arXiv:1208.4670), doi:10.1117/12.924507
- Kumar A., Ghosh S. K., et al. 2012b, in *Space Telescopes and Instrumentation 2012: Ultraviolet to Gamma Ray*. p. 84434R (arXiv:1208.4672), doi:10.1117/12.924147
- Kumar R., Pradhan A. C., Parthasarathy M., Ojha D. K., Mohapatra A., Murthy J., Cassisi S., 2020a, arXiv e-prints, p. arXiv:2012.07318
- Kumar R., Pradhan A. C., Parthasarathy M., Ojha D. K., Mohapatra A., Murthy J., 2020b, in Bragaglia A., Davies M., Sills A., Vesperini E., eds, *IAU Symposium Vol. 351, Star Clusters: From the Milky Way to the Early Universe*. pp 464–467 (arXiv:1908.02512), doi:10.1017/S1743921319007373
- Lagioia E. P., Dalessandro E., Ferraro F. R., Salaris M., Lanzoni B., Pietrinferni A., Cassisi S., 2015, *The Astrophysical Journal*, **800**, 52
- Lee K. H., Lee H. M., Fahlman G. G., Sung H., 2004, *AJ*, **128**, 2838
- Marino A. F., et al., 2014, *MNRAS*, **437**, 1609
- Massari D., Koppelman H. H., Helmi A., 2019, *A&A*, **630**, L4
- Moehler S., 2010, *Mem. Soc. Astron. Italiana*, **81**, 838
- Moehler S., Landsman W., Napiwotzki R., 1998, *A&A*, **335**, 510
- Moehler S., Landsman W. B., Lanz T., Miller Bertolami M. M., 2019, *A&A*, **627**, A34
- Muñoz R. R., Côté P., Santana F. A., Geha M., Simon J. D., Oyarzún G. A., Stetson P. B., Djorgovski S. G., 2018, *ApJ*, **860**, 65
- Navarrete C., Belokurov V., Koposov S. E., 2017, *ApJL*, **841**, L23
- Parthasarathy M., Jasniewicz G., Aoki W., Takeda Y., 2012, in Aoki W., Ishigaki M., Suda T., Tsujimoto T., Arimoto N., eds, *Astronomical Society of the Pacific Conference Series Vol. 458, Galactic Archaeology: Near-Field Cosmology and the Formation of the Milky Way*. p. 237
- Piotto G., et al., 2015, *AJ*, **149**, 91
- Posti L., Helmi A., 2019, *A&A*, **621**, A56
- Postma J. E., Leahy D., 2017, *PASP*, **129**, 115002
- Rahna P. T., Murthy J., Safonova M., Sutaría F., Gudennavar S. B., Bubbly S. G., 2017, *MNRAS*, **471**, 3028
- Riffel R., Ruschel-Dutra D., Pastoriza M. G., Rodríguez-Ardila A., Santos J. F. C. J., Bonatto C. J., Ducati J. R., 2011, *MNRAS*, **410**, 2714
- Rosenberg A., 2000, *PASP*, **112**, 575
- Sahu S., Subramaniam A., Côté P., Rao N. K., Stetson P. B., 2019, *MNRAS*, **482**, 1080
- Sarajedini A., et al., 2007, *AJ*, **133**, 1658
- Schiavon R. P., et al., 2012, *AJ*, **143**, 121

- Shapley H., 1918, [Publications of the Astronomical Society of the Pacific](#), 30, 42
- Shapley H., 1920, [ApJ](#), 52
- Shapley H., Sawyer H. B., 1927, Harvard College Observatory Bulletin, 849, 11
- Stetson P. B., Pancino E., Zocchi A., Sanna N., Monelli M., 2019, [MNRAS](#), 485, 3042
- Subramaniam A., Tandon S. N., et. al. 2016, in Space Telescopes and Instrumentation 2016: Ultraviolet to Gamma Ray. p. 99051F ([arXiv:1608.01073](#)), [doi:10.1117/12.2235271](#)
- Subramaniam A., et al., 2017, [AJ](#), 154, 233
- Tandon S. N., Subramaniam A., Girish V., et. al. 2017, [AJ](#), 154, 128
- Tandon S. N., et al., 2020, [AJ](#), 159, 158
- Tenorio-Tagle G., Muñoz-Tuñón C., Cassisi S., Silich S., 2016, [ApJ](#), 825, 118
- Tenorio-Tagle G., Silich S., Palouš J., Muñoz-Tuñón C., Wünsch R., 2019, [ApJ](#), 879, 58
- Vanderbeke J., et al., 2014, [MNRAS](#), 437, 1725
- Vasiliev E., 2019, [MNRAS](#), 484, 2832
- Villanova S., Geisler D., Piotto G., Gratton R. G., 2012, [ApJ](#), 748, 62
- Zinn R. J., Newell E. B., Gibson J. B., 1972, [A&A](#), 18, 390

This paper has been typeset from a $\text{\TeX}/\text{\LaTeX}$ file prepared by the author.